
Grating Inspection System for Large-Scale Multilayer-Dielectric Gratings for High-Energy Laser Systems

Introduction

The OMEGA EP Laser System at LLE is a petawatt-class laser system capable of producing high-energy laser pulses with lengths shorter than a picosecond. Short-pulse production is achieved in a pulse compressor composed of large-aperture (meter-scale) multilayer-dielectric diffraction gratings.¹ The pulse compressor consists of four tiled-grating assemblies (TGA's) within a vacuum grating compressor chamber (GCC).² The fourth TGA handles the highest compressed power and is, therefore, most prone to laser-induced damage, requiring frequent inspection. A grating inspection system (GIS) has been developed to provide *in-situ* detection of potential damage features on the fourth TGA without disturbing the vacuum environment or the alignment of the TGA's.

In this article we describe the GIS, which provides high-resolution damage-sensitive imaging of the diffraction grating's optical surface. Selective sensitivity to damage is achieved by using a dark-field imaging system that collects scattered (as opposed to reflected or diffracted) light from the optical surface. This technique is not, in principle, dependent on the diffractive nature of the surface under test and should be applicable to any flat optical surface that causes minimal scattering when in an undamaged state.³

This article will (1) discuss the GIS system with design requirements and constraints; (2) present an alignment method that optimizes performance; (3) discuss the background and thermal issues that arise from using the GIS system in a vacuum environment; (4) present a data-reduction scheme that addresses various unique issues posed by the system; (5) demonstrate measurement results obtained from the GIS during a recent energy ramp campaign; and (6) present conclusions.

System Description

A number of key requirements were imposed on the GIS system design to ensure compatibility with the OMEGA EP pulse compression system:

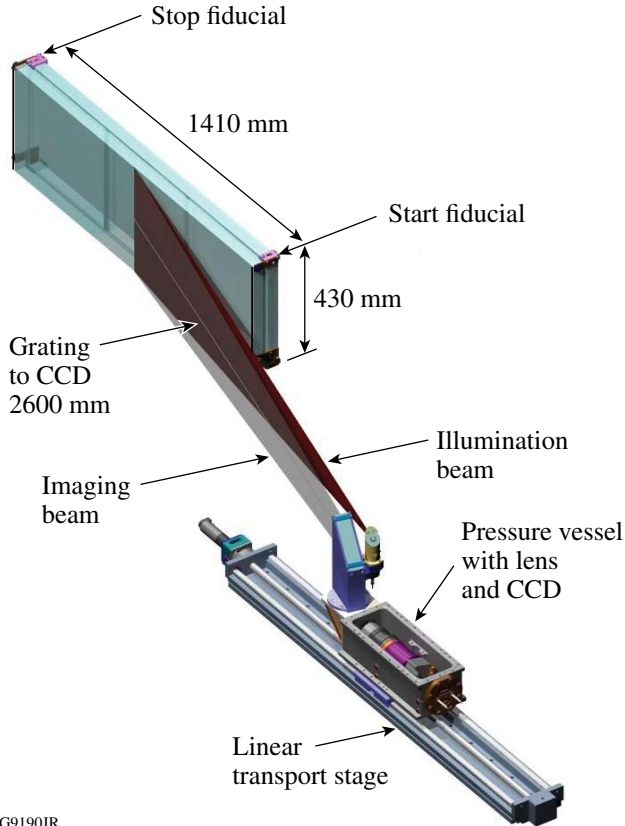
1. The GIS may not enter a volume assigned to any other GCC devices.
2. The GIS must not obstruct shot and alignment beams.
3. GIS heat output must be less than 1 W/h per measurement.
4. All material must be rated as vacuum compatible and satisfy class-100-level cleanliness requirements.
5. GIS must be capable of detecting damage features as small as 250 μm .

To best satisfy these requirements, a linearly scanned, dark-field imaging concept was selected. A scanning system allows one to sample a number of object points greater than the number of pixels on the sensor, which is a significant advantage over other design concepts given the size of the object to be imaged ($\sim 6 \times 10^5 \text{ mm}^2$) and the feature size requirement [see requirement (5) above]^a. In the context of imaging a highly angle dependent surface such as a diffraction grating, a scanning system has the additional advantage that the viewing angle is constant with respect to position along the scan-parallel direction.

The GIS consists of three subsystems: (1) a line-illumination system, (2) a line-imaging system aligned to view the illuminated portion of the grating surface, and (3) a transport mechanism that scans these across the width of the TGA to form a two-dimensional image. Figure 124.1 shows an overview of the system, and Table 124.I outlines the specifications of the as-built system, which satisfies the design requirements.

The illumination system consists of a line generator that projects an elongated Gaussian pattern onto the grating surface.

^aNote that requirement (5) concerns *detection*, not *resolution*. It is invoked here only as an estimator of the required resolution and, in turn, the required number of object plane samples.



G9190JR

A line generator is used rather than a simpler area illumination concept to provide sufficient irradiance in the region imaged by the camera, while requiring only a modest total power. Light is provided by a 1053-nm fiber laser external to the GCC and transported to the line generator via a single-mode, polarization-maintaining fiber. Since both high illumination intensity and a long optical fiber to deliver illumination to the GIS are required, special care was necessary to prevent stimulated Brillouin scattering from destroying the fiber. This was achieved by using a custom fiber-laser source with a relatively short coherence length as compared to commercial products at this wavelength.

As closely as possible, the illumination light matches the polarization (vertical), incidence angle ($\sim 72^\circ$), and wavelength (1053 nm) for which the gratings are designed to exhibit their highest diffraction efficiency. Mechanical restrictions on the location of the GIS within the GCC [see requirement (1) above] preclude, however, an exact match to the desired angle of incidence. As a compromise, an angle of incidence of 78.5°

Figure 124.1

Grating inspection system is shown scanning across a 1.41-m \times 0.43-m tiled-grating assembly. Note that the pressure vessel housing cover is absent in this image for illustrative purposes.

Table 124.I: System parameters.

Imaging System	
Working (object) distance	2.6 m
Viewing angle w.r.t grating surface	76°
Focal length	250 mm
Full field of view	14°
Feature detection	$250 \mu\text{m}$ or larger
Sensor	Dalsa Piranha 2 8192-pixel array, 10 bits/pixel, $7\text{-}\mu\text{m}$ pixel size
Lens	Mamiya KL 4.5/250L-A (Ref. 4)
Illumination	
Wavelength	1053 nm
Angle of incidence	78.5° from surface normal
Power at line generator	180 mW
Line shape on grating surface	Gaussian $1 \times 500 \text{ mm}$ at $1/e^2$
Mechanical	
Alignment fiducial	$250\text{-}\mu\text{m}$ -diam acid-etched wires, coplanar with grating surface
Vacuum-compatible reticulating stage	Straightness = $100 \mu\text{m}$ over 1.5 m, effective drive/encoder resolution = $2 \mu\text{m}$

from the grating surface normal is used. This is close enough to the ideal angle that diffraction efficiency is not significantly affected. Most of the incident light is therefore diffracted, minimizing stray light from reflections in the grating substrate or nearby mechanical components. Light striking a damaged portion of the grating will be diffracted less efficiently, leading to scatter that may be detected by the imaging system.

The imaging system consists of a commercial medium-format photographic lens that images the optic surface to a linear charge-coupled-device (CCD) array camera. The camera captures light from one vertical strip of the optic during each acquisition, building an image as the scanner moves horizontally across the TGA surface. The camera and imaging lens are housed in an airtight case, along with temperature and pressure sensors. This casing preserves atmospheric pressure to facilitate heat dissipation from the camera (see **Mitigation of Thermal and Background Effects**, p. 168) and to prevent contamination of the GCC by outgassing from the camera, lens, or associated electronics. A periscope assembly, external to the airtight case, keeps the camera and imaging lens out of the on-shot and alignment beam envelopes. Figure 124.2 gives an overhead view of the GIS camera and pressure vessel including the periscope and illumination and imaging systems.

The imaging lens provides a reduction from object to image by a factor of 8.9, mapping the $7\text{-}\mu\text{m}$ pixels of the camera to about $62.5\ \mu\text{m}$ in the object plane.⁴ The camera views the grating surface at a shallow angle, however, which spreads the object space footprint of each pixel by a factor of 3.8 in the horizontal direction, covering an area of $62.5 \times 237.5\ \mu\text{m}$ in the plane of the grating surface. The GIS typically acquires

a line of data per $16\ \mu\text{m}$ of travel across the grating surface, which, in combination with the horizontal extent of the pixel footprint in object space, means that every point on the grating surface contributes to the signal in adjacent lines of data in the output image. Acquiring data in this way provides a low-pass effect and strong oversampling, which is an advantage in data reduction for reducing noise and eliminating a particular type of image defect (see **Data Reduction**, p. 169).

The linear transport is parallel to the surface of the grating and offset from it along the scan direction. The placement of the GIS transport was chosen to accommodate existing GCC equipment and satisfied the top-level requirements. Custom drive electronics for the linear transport provide a trigger signal for the camera, which is synchronized to the rotary encoder output from the drive motor. This prevents fluctuations in transport velocity from producing distortions in the image data and ensures that the scale of the image will be highly repeatable.

Installation and Alignment

To maximize the sensitivity of the GIS, the illumination line and the line imaged by the CCD must overlap precisely. Using a high-precision coordinate measuring machine,⁵ the transport stage was aligned to be parallel to the grating surface at the correct distance to yield a nominal viewing angle of 14° relative to the scan direction (76° relative to the grating surface normal). This angle was mandated by the mechanical constraints discussed in the previous section. To facilitate the alignment between illumination and imaging beams, alignment fiducials are installed on the TGA for use with the GIS. The fiducials are $250\text{-}\mu\text{m}$ -diam stainless-steel wire, strung 3 mm from the edge of the grating, parallel to the edge, and copla-

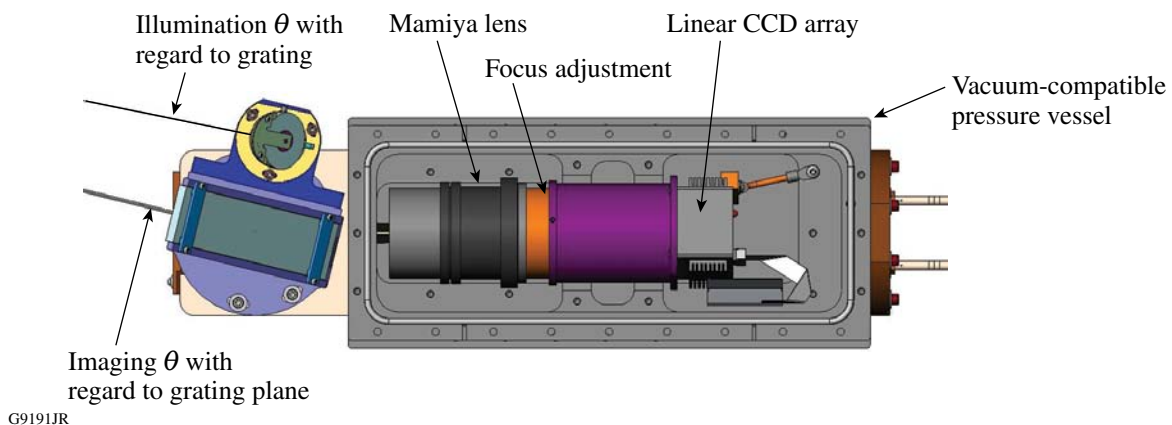


Figure 124.2

An engineering top-view drawing shows the vacuum-compatible pressure vessel housing the major components of the imaging system. This reduces contamination and out-gassing while keeping the camera functioning in air. The separation between illumination and imaging is also indicated.

nar with the grating surface. They are imaged in every GIS scan, providing information on the GIS alignment and focus state and verification that the illumination source is functioning properly. The fiducials also play an important role in the installation and alignment of the GIS, where they serve as a reference for the rotation and pointing of both the camera and the illumination line.

Alignment was achieved using the following procedure: First, the top and bottom of the fiducial wire were illuminated with small “marker” beams from a HeNe laser. With the camera moved to the limit of travel corresponding to the illuminated fiducial, the periscope was tipped and tilted until the HeNe illumination was detected and centered on the CCD. The camera was then rotated to bring both HeNe illuminated portions of the fiducial into view. Next, the 1.053- μm line generator was added and pointed at the fiducial wire. The line had to be rotated to be within the field of view of the linear CCD array, corresponding to a 120- μrad tolerance. Finally, the focus and polarization of the line generator were checked to maximize the return signal and minimize transmitted light through the grating, respectively. These alignment steps had to be iteratively repeated until the desired signal level was achieved.

Mitigation of Thermal and Background Effects

The GIS camera generates a significant quantity of heat whenever it is receiving power and suffers from severely limited thermal dissipation because it operates in a vacuum environment. This creates a number of consequences when operating the instrument: Unnecessary thermal pollution of the GCC by the GIS can impact the optical alignment of the grating compressor, which must be avoided. The CCD temperature can vary strongly over the scan duration of roughly 8 min, which directly influences the dark current background. Finally, the long-term equilibrium temperature of the camera, while energized, is potentially damaging to the CCD.

The pressure vessel housing the camera mitigates these effects to some degree by providing a significant thermal mass in close contact with the camera, while the vessel itself remains in poor contact with the GCC as a whole. Thermal effects, however, must also be minimized procedurally.

A study of the thermal behavior of the GIS was conducted during installation within the vacuum GCC, which was used as a guide in developing a set of usage protocols that mitigate thermal effects. Data were continuously acquired from the GIS camera for roughly 45 min, and the temperature was recorded from an in-camera thermistor. Temperature data were collected

once per 500 lines of image data at a 0.5 °C resolution. A model function was fitted to the data, consisting of a single exponential function rounded to the nearest half-degree. Figure 124.3 shows the raw data and the rounded-fit function, as well as the exponential component of the model, before rounding.

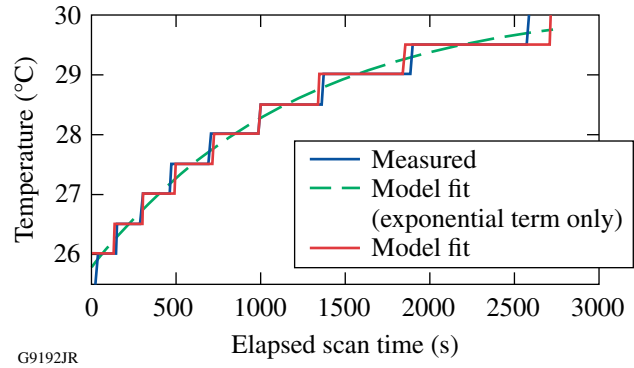


Figure 124.3

Measured temperature, fitted-model data, and the exponential component of the fitted model.

The exponential component of the fitted model is used to estimate the temperature, from which a value is interpolated to correspond with each line of image data. Figure 124.4 shows the background level versus temperature for each line of data from the CCD. This establishes a thermal variation of the background of 2.0 counts/degree.

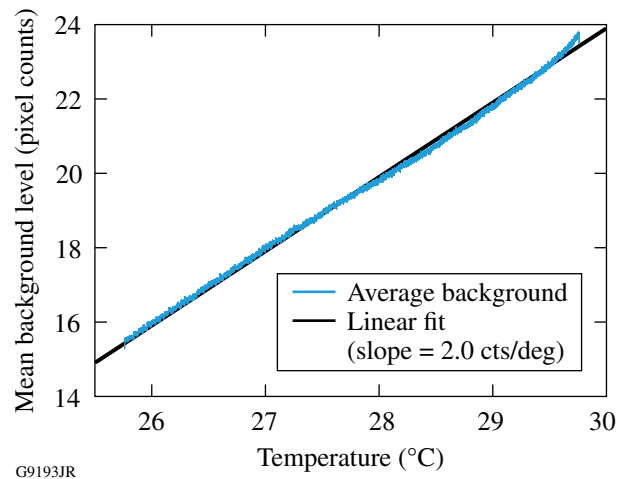


Figure 124.4

Mean background level versus temperature during the thermal study.

Over an 8-min scan, the rise in temperature could be many degrees, which would produce unacceptable variations in background. This is mitigated in GIS operation by a series of operations carried out by the GIS acquisition software. When

a scan is initiated by the user, this software ensures that the camera is at or above 23 °C to reduce the second derivative of the temperature with respect to time. If the camera is below this temperature, it is energized and warmed up before the scan is initiated. Once scanning begins, 500 lines of image data are acquired to provide pre-scan background data. Post-scan background is similarly measured immediately after the scan is concluded. The pre- and post-scan background data are used quite effectively by the GIS data-reduction algorithms to compensate for variation in the background, as described in the next section. The variance in the background will, of course, also increase with temperature; this variation has been undetected in testing, however, and is assumed to be negligible.

Data Reduction

Raw data from the GIS, as from practically all imaging systems, have a number of undesirable characteristics that must be corrected during data reduction to provide the most-accurate possible representation of the surface being inspected. Some characteristics of the GIS data are relatively unique, and their treatment will be described in detail. Double exposures (DE's) are the most notable of these because of their strong impact on image quality if uncorrected. DE errors, as they occur in a scanning system like the GIS, are quite unique and cannot be corrected using basic image-processing techniques, such as smoothing or filtering. The GIS data reduction also performs background subtraction, which is, in principle, a common operation. However, because of the thermally induced background variation over the duration of a GIS scan, this process is carried out in a somewhat unique manner. Finally, the GIS data reduction must correct for the nonuniform illumination level, which varies strongly across the vertical extent of the image as a result of the Gaussian shape of the illumination line.

DE's are caused by a known issue in the trigger logic of the Dalsa Piranha2 camera when running at line rates below 1 kHz. During a DE, the camera fails to respond to a trigger signal,

resulting in a line of data being exposed for two integration periods. DE's are relatively infrequent; it is typical to gather a full scan (roughly 88,000 lines) without a single occurrence. An uncorrected DE would be problematic, however, for later analysis and must be removed. DE's are corrected by inspecting the column sums of a region at the top of the GIS image. The region spans the full image, is 400 pixels tall, and was chosen for its absence of any significant image features (i.e., it is dominated by background). Figure 124.5 identifies this region.

The column sums are divided by a median-filtered copy of themselves, and DE's are identified by points where this ratio exceeds six standard deviations above its mean value. Figure 124.6 displays the column sums and the same data after a median filter. DE reduction in this manner is highly effective because the median filter is ideal for identifying isolated extreme values in the raw data.

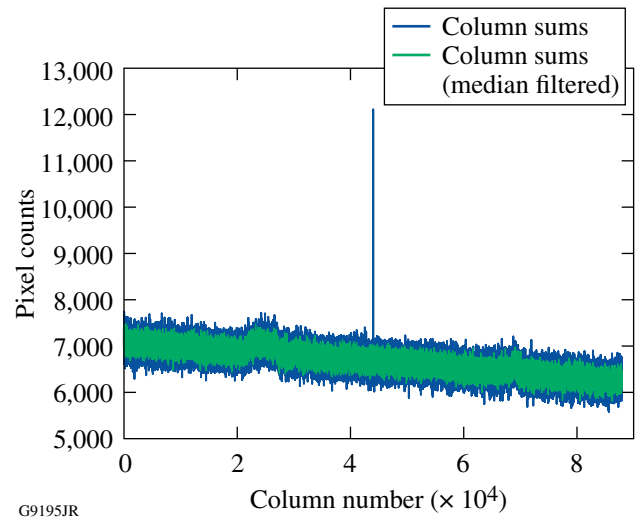


Figure 124.6 Column sums of the image data in the region of interest are shown. A DE is simulated at line 40,000 because real DE's are very infrequent.

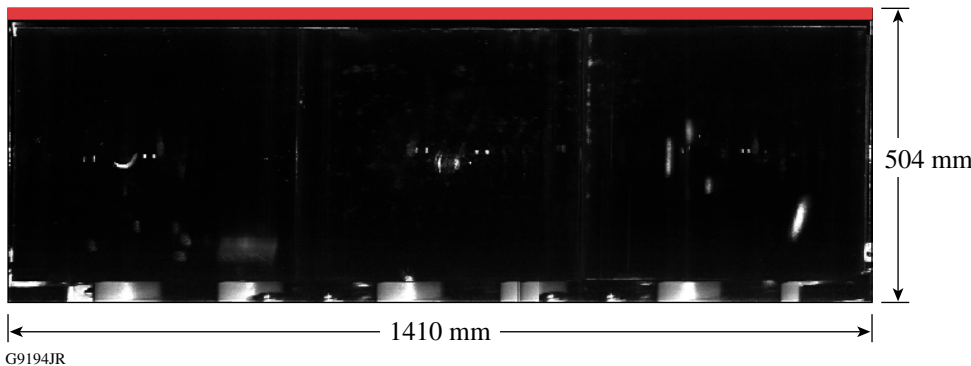


Figure 124.5 A typical GIS image (the region used to detect DE is identified in red).

Once identified, columns affected by a DE are eliminated and replaced with interpolated values from their neighboring columns. This interpolation is justified in this case by the large oversampling in the horizontal (scan) direction. As described in **System Description** (p. 165), the pixel footprint in the plane of the grating has a horizontal extent of roughly $237.5 \mu\text{m}$, while acquisition occurs every $16 \mu\text{m}$. This implies that 93% of the area imaged by each pixel is also imaged in each of the adjacent data lines, making interpolation between adjacent pixels highly reliable.

After correcting DE's in the image data and in the pre- and post-scan background data by the same process, the data reduction corrects for the variable background level. The background values are interpolated linearly across the GIS image from the pre-scan to the post-scan levels, and these interpolated values are subtracted from the image. In effect, this assumes that the background level increases linearly with time as the scan progresses, which of course, it does not. However, because the second derivative of the temperature change versus time has been constrained by the data acquisition process (see **Mitigation of Thermal and Background Effects**, p. 168), the deviation of the background from the linear interpolation is also bounded. Figure 124.7 shows the exponential model for the temperature data, extrapolated to the 7-min period immediately after the camera reaches $23 \text{ }^\circ\text{C}$. The start-to-end linear approximation deviates from the exponential by a maximum of $\sim 0.09 \text{ }^\circ\text{C}$, which translates into a maximum error in the background estimation of roughly 0.18 CCD counts. This subcount departure should be insignificant to further image processing and will be even smaller if the scan begins at a temperature higher than

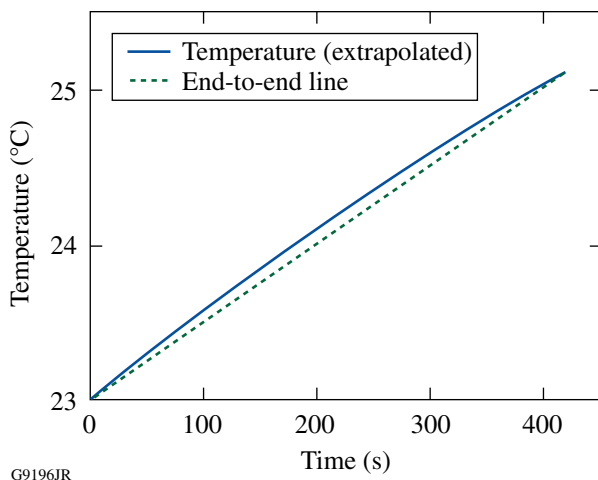


Figure 124.7
Temperature data are shown extrapolated over the travel scan time.

$23 \text{ }^\circ\text{C}$, where the exponential behavior of the temperature is more closely approximated by a line.

Finally, the data reduction corrects for strong variations in signal strength across the vertical extent of the image, such as from illumination nonuniformity. This variation would confound any image analysis based on a fixed binarization threshold. To correct the signal level, an equalization coefficient is applied to the data from each pixel of the CCD array. Equalization coefficients are calculated from a GIS scan of a reference surface, which is collected during installation and maintenance of the GIS. The reference surface is a uniform scattering surface composed of white Delrin.⁶ Note that this measurement includes more than just the Gaussian shape of the illumination. By using measured data from the GIS, rather than a pre-characterization of the illumination profile, this equalization also accounts for variations in photoresponse for each pixel, vignetting in the imaging lens, and other properties of the as-built system.

Figure 124.8 shows the measured equalization coefficient for each pixel in the CCD array, demonstrating that the Gaussian illumination profile clearly dominates other effects. It must be noted that the scattering properties of the reference target and of scattering sites on the optic being imaged are certainly non-Lambertian and likely not identical. It is unclear to what extent this distorts the equalization coefficients, but it is assumed to be negligible. It is also important to understand that equalizing the signal level cannot alter the signal-to-noise ratio, which inevitably varies across the vertical dimension of the image.

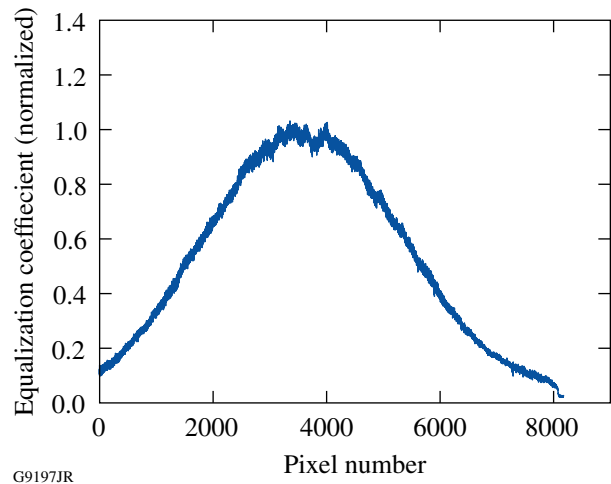


Figure 124.8
Signal equalization coefficients for each pixel in the CCD array.

A 3×3 median filter is applied to the image to suppress noise. Median filtering typically provides good noise suppression without compromising image detail as heavily as, for example, a smoothing filter. A median filter is particularly effective on GIS images at this point because, as discussed above, they are heavily oversampled in the horizontal direction. So, the noise suppression from the median filter comes at the cost of virtually no loss of image structure in the horizontal direction and acceptable loss in the vertical direction.

At this point the anomalies in the GIS data are sufficiently corrected to give an image that represents, as accurately as possible, the scattering sites on the optic under test. The final step in data reduction is to re-scale the GIS image to a standard pixel scale of 16 pixels/mm. This simplifies future processing and measurements and offers an opportunity for further noise suppression. The scale factors for this transformation are determined to sufficient precision by measuring the size of a known feature in a raw GIS image, such as the outline of a grating tile. Raw GIS data have a scale of roughly 61.26 and 16.25 pixels/mm in the horizontal and vertical directions, respectively. The image is re-scaled via bi-cubic interpolation with an anti-aliasing filter.⁷

Results

The GIS allows one to make frequent *in-situ* measurements of the TGA surface. The optics are also inspected visually during semi-annual maintenance periods when the GCC is vented to atmospheric pressure. This visual inspection is the conventionally accepted method for observing morphological change (MC) on optical surfaces and serves as a performance benchmark for the GIS in terms of sensitivity to damage features. Visual inspection also provides a point of comparison for determining whether all MC's that appear under visual inspection are detected by the GIS. Figure 124.9 compares (a) a photograph of a damaged region of a grating taken during visual inspection and (b) the same region as imaged by the GIS.

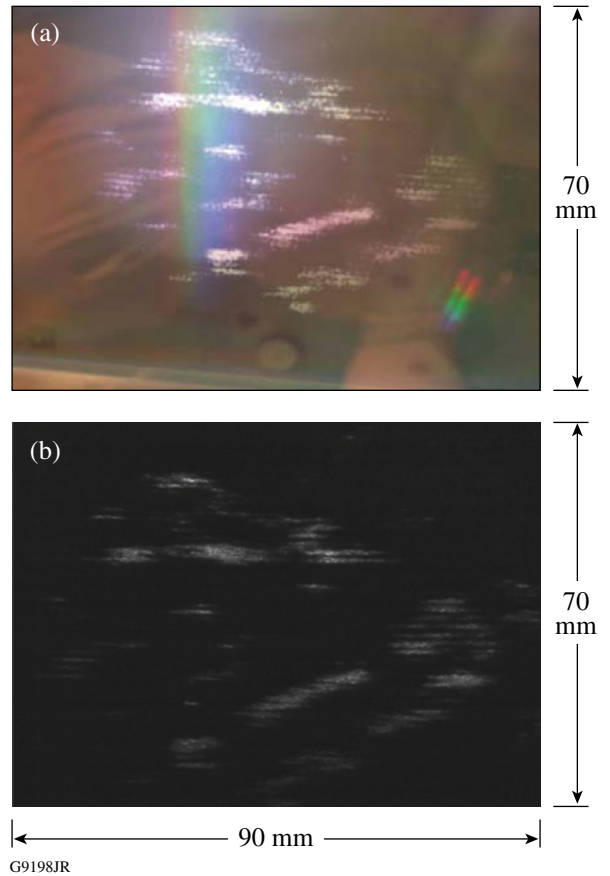


Figure 124.9
 (a) A photograph taken during visual inspection on 19 June 2009 and (b) the same region of the TGA surface imaged by the GIS on 7 September 2009. Clear correlation can be seen between the surface features detected by both methods.

Such correspondence between GIS observations and visual inspections has now been repeatedly supported and represents an important measure of the success of the GIS.

Final output from the GIS is a high-quality, high-resolution image ready to use to identify and analyze damage on the TGA surface. Figure 124.10 shows a typical image. Note that in this

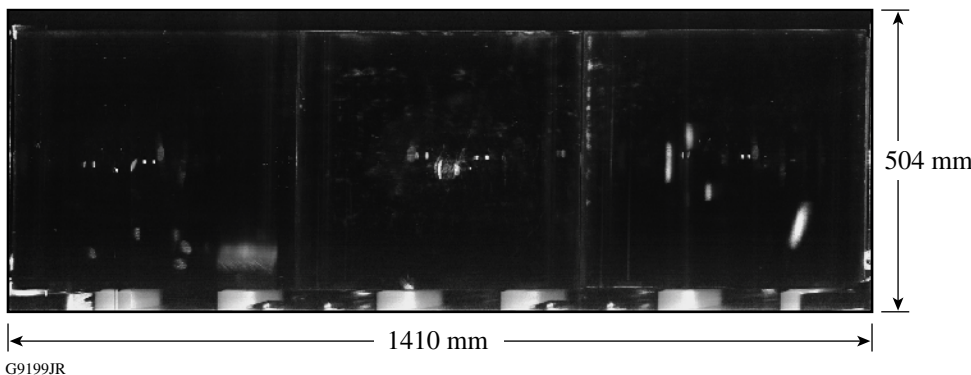


Figure 124.10
 A typical image of a TGA as produced by the GIS. A variety of common non-damage features are visible.

image, and most others presented in this article, the contrast has been significantly adjusted to make details visible to the reader. In their original state, for use in analysis, the dynamic range of the GIS is very large, and much of the interesting structure is present at the lower end of the intensity scale. The TGA was in good condition at the time of the scan in Fig. 124.10, and very little scattering was present from damage or other MC on the optical surface. Therefore, this image is a good illustration of the “background” features in a “pre-damaged” GIS image. In the central region of each grating tile can be observed two pairs of bright circular features, in some cases with another one or two larger oval-shaped features between them. These are inherent to the grating tiles and are not fully understood. They are not visible under human inspection of the gratings. The inter-tile gaps are clearly visible, as well as the fiducial wires at the extreme edges of the image. A number of other optical ghosts are visible, generally appearing as oblong “blemishes.” Some of these ghosts are assumed to be stray-light artifacts, possibly resulting from some part of the TGA mechanical assembly. Finally, along the bottom of the image, one can observe a portion of the TGA mechanical structure. Particularly prominent

here are the six white rectangular features that result from a set of Delrin cylinders on the TGA support structure. Recognizing and measuring these background features are vital to any analysis seeking to identify MC on the grating surface. Clearly, it is necessary to employ techniques that compare a potentially damaged grating to an earlier reference. These analysis methods, however, are beyond the scope of this article.

The GIS has been highly successful in detecting MC attributable to high-energy operation of the OMEGA EP system. Figure 124.11 shows a GIS image gathered after a recent energy-ramp campaign. Even without rigorous analysis, MC is clearly visible in the lower portion of the center tile and the upper-right quadrant of the left tile. The region highlighted by the red box contains the two most-severe MC’s on the grating surface, with severity being judged by the surface area of the MC.

The progression of this damage can be investigated in greater detail. Figure 124.12 shows a sequence of images of this region at full resolution, demonstrating the progression of MC during the energy ramp.

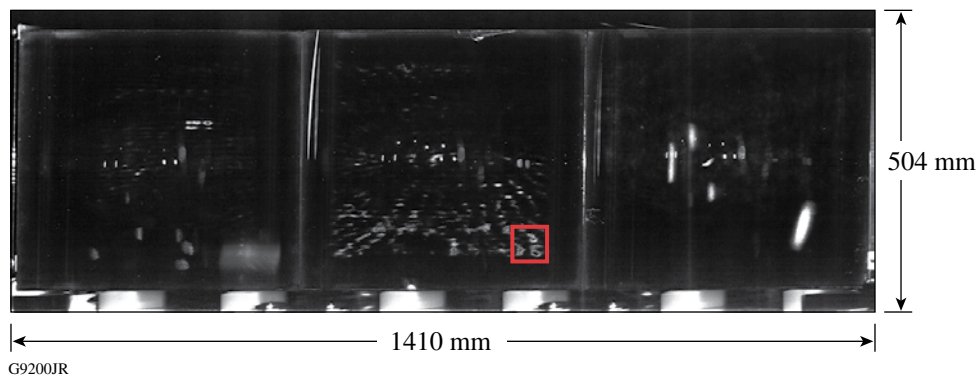


Figure 124.11

GIS image taken after the final shot in the OMEGA EP energy-ramp campaign. Damage-induced scattering is visible in multiple areas. The area outlined in red highlights the two most severely damaged sites in terms of affected area.

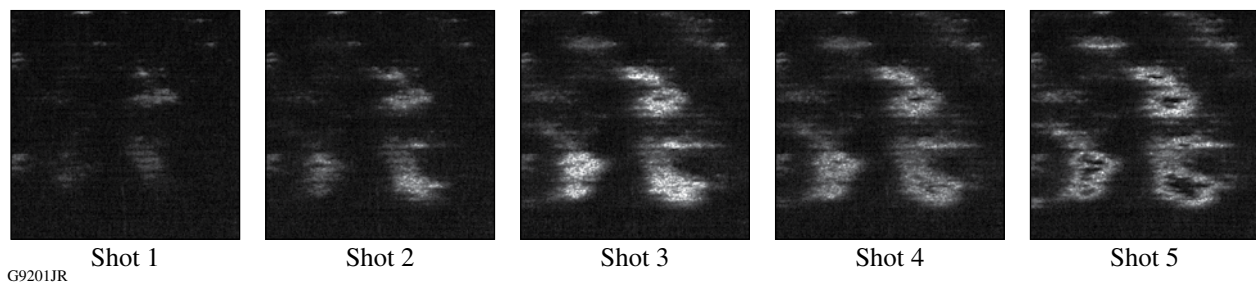


Figure 124.12

A progression of images of a region of the final TGA in the OMEGA EP upper compressor during the energy-ramp campaign. This is the region identified in Fig. 124.11.

It is interesting to note that, as MC's progress, the scattering signal becomes stronger until a point is reached (shot 3) at which the scattering signal is abruptly reduced. This effect becomes visible on shot 4 and is dramatically apparent on shot 5. Subsequent analysis of this and other regions of the grating tile using an atomic force microscope reveal that, in the region where scattering has ceased, the pillars comprising the diffractive surface structure have been completely ejected from the surface.

Conclusion

The grating inspection system has been integrated into the OMEGA EP vacuum grating compression chamber. It operates reliably within the allowed operational window between shots and has successfully demonstrated the ability to detect features in the specified 250- μm scale. Statistical techniques have been applied to GIS observations to establish system fluence limits that minimize the threat of damage to the gratings, while making it possible for OMEGA EP to satisfy its short-pulse mission.⁸ There is great potential for further investigation of the *in-situ* behavior of large-aperture diffraction gratings, and the GIS will continue to play a vital role in this work.

ACKNOWLEDGEMENT

This work was supported by the U.S. Department of Energy Office of Inertial Confinement Fusion under Cooperative Agreement No. DE-FC52-08NA28302, the University of Rochester, and the New York State Energy Research and Development Authority. The support of DOE does not constitute an endorsement by DOE of the views expressed in this article.

Special thanks to LLE software engineers Steve Smith and Mark Wilson and LLE electrical engineer Scott Ingraham for their excellent work and support in developing the GIS image acquisition software and drive electronics. We also extend thanks to system scientist Jie Qiao, optical engineer Damon Diehl (ASE Instrument, Inc.), and LLE engineering director/chief safety officer Dr. D. W. Jacobs-Perkins for their great guidance and support.

REFERENCES

1. T. J. Kessler, J. Bunkenburg, H. Huang, A. Kozlov, and D. D. Meyerhofer, *Opt. Lett.* **29**, 635 (2004).
2. J. Qiao, A. Kalb, M. J. Guardalben, G. King, D. Canning, and J. H. Kelly, *Opt. Express* **15**, 9562 (2007).
3. M. Commandré, in *Laser-Induced Damage in Optical Materials: 2008*, edited by G. J. Exarhos *et al.* (SPIE, Bellingham, WA, 2008), Vol. 7132, p. 713200.
4. This lens is listed as $f/4.5$, EFL = 250 mm. The mechanical requirements of the pressure vessel housing impose, however, a number of noncircular apertures. In practice, this system has different effective apertures in the vertical and horizontal directions and is likely slower, overall, than $f/4.5$.
5. FARO Technologies, Inc., Lake Mary, FL 32746 (<http://www.faro.com>).
6. McMaster Carr Supply, Aurora, OH 44202 (<http://www.mcmaster.com>).
7. See MATLAB 7.8.0.347 documentation for the image resize function in the Image Processing Toolkit.
8. J. Qiao, A. W. Schmid, L. J. Waxer, T. Nguyen, J. Bunkenburg, C. Kingsley, A. Kozlov, and D. Weiner, *Opt. Express* **18**, 10,423 (2010).